



Comparison of NIST SA13a and SA4b SQUID Array Amplifiers

Maximiliano Silva-Feaver¹  · Kam Arnold¹ · Darcy Barron¹ · Edward V. Denison¹ · Matt Dobbs¹ · John Groh¹ · Gene Hilton¹ · Johannes Hubmayr¹ · Kent Irwin¹ · Adrian Lee¹ · Leila R. Vale¹

Received: 6 November 2017 / Accepted: 17 August 2018 / Published online: 17 September 2018
© Springer Science+Business Media, LLC, part of Springer Nature 2018

Abstract

Several current and proposed cosmic microwave background experiments use transition edge sensor bolometer focal planes coupled to the digital frequency-domain multiplexing (DfMux) electronics. This readout architecture sums bolometer signals in a SQUID array amplifier (SAA). In this study, we investigate the properties of two SAA designs, the SA4b, which is currently used in the DfMux system, and the SA13a. The SA13a design is gradiometric, making it less sensitive to stray magnetic field pickup. It has lower input inductance and is laid out on the chip as a re-configurable array with 6 banks of 64 series SQUIDs that can be arranged in any series and parallel configurations to optimize array noise, peak-to-peak modulation depth, and dynamic output resistance. The SA13a design reported on here is configured with 3 banks in series \times 2 banks in parallel. The SA4b is a series array of 100 SQUIDs in series, each with an 8-turn input coil.

Keywords SQUID · CMB · TES bolometer · Multiplexing

1 Introduction

Since the deployment of the first frequency-domain multiplexing (fMux) system for Transition Edge Sensor (TES) bolometer readout on the APEX-SZ cosmic microwave background (CMB) experiment [1], which used the National Institute of Standards and Technology (NIST) SA4b [2] Superconducting Quantum Interference Device (SQUID) Array Amplifier (SAA), there have been innovations in SAA design and there are a number of existing and upcoming CMB experiments using the fMux architecture

✉ Maximiliano Silva-Feaver
msilvae@ucsd.edu

¹ Department of Physics - Center for Astrophysics and Space Sciences, University of California San Diego, La Jolla, CA 92093, USA

[1,3–7]. This is an initial study of two designs, aimed at guiding a more complete optimization of SAA design for the Digital Frequency-Domain Multiplexer (DfMux) [8] and to provide public data on two commonly used NIST SAA designs. The SAA implementation in the most recent DfMux system is shown schematically in Fig. 1 and in pictures in Fig. 2. It provides the necessary amplification of the bolometers' amplitude-modulated current signal (carrier frequencies in the 1–5 MHz band), while injecting sub-dominant noise itself and providing a low-impedance input in series with the voltage-biased TES bolometer.

The general definition of a SQUID is a nonlinear superconducting circuit element consisting of a superconducting loop interrupted by one or more Josephson junctions [9]. SQUID Array Amplifiers (SAAs) are built out of DC SQUIDS which have 2 Josephson junctions. If the DC SQUID is current biased, it will exhibit a periodic (not purely sinusoidal) voltage across the Josephson junctions as a function of magnetic flux through the SQUID loop due to flux quantization and Josephson tunneling. The peak-to-peak amplitude of this oscillation is a function of the current bias applied as shown by the red curve in Fig. 3a. To form an SAA, multiple DC SQUIDS are arrayed in series and parallel. Series combinations increase the gain and dynamic impedance (output impedance) while decreasing the input-referred noise. Parallel combinations

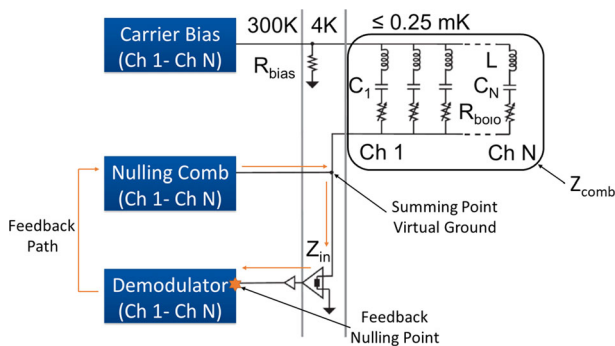


Fig. 1 Schematic diagram of the DfMux TES bolometer multiplexing scheme. The amplifier shown at 4 K is the SAA. Z_{in} is the input impedance of this amplifier, and Z_{comb} is the impedance of the sub-Kelvin part of the circuit, including the parallel bank of detectors and their associated LC filters (Color figure online)

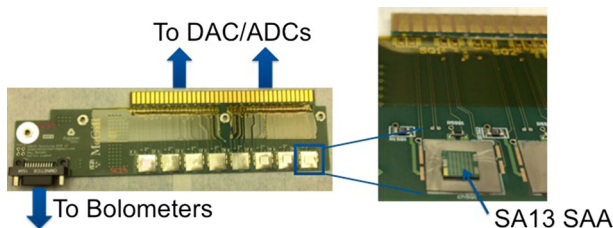


Fig. 2 Left: SQUID mounting board used in DfMux readout system. Arrows indicate connections to room-temperature digitizers and cryogenic bolometers. Right: a SA13a SAA mounted on a SQUID mounting board. It is mounted on top of niobium foil, which shields against magnetic field variation once the niobium has transitioned into its superconducting state. Upon integration, this card is surrounded in a high-permeability shield to decrease magnetic interference from the environment (Color figure online)

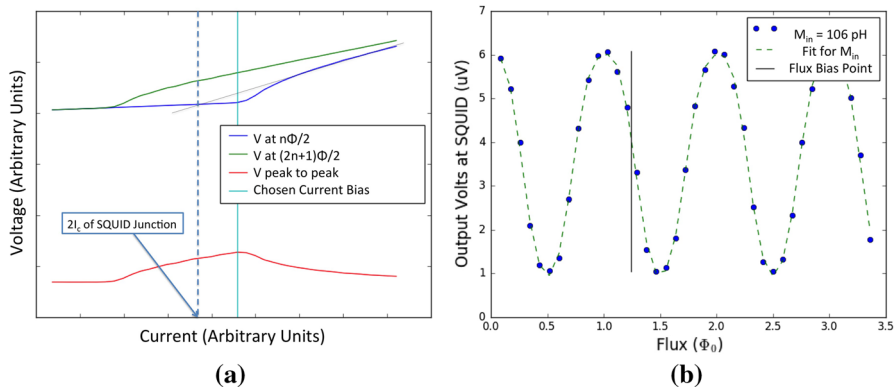


Fig. 3 **a** Characteristic IV curve showing how to find the critical current of the SQUID (intersection of the gray line with $V = 0$), the behavior of V_{pp} of the $V-\Phi$ response as a function of bias current, and identification of our current bias tuning point. **b** A characteristic $V-\Phi$ response of a SQUID with our flux bias point shown (Color figure online)

reduce the output impedance, decrease the input-referred noise, but do not change the gain. Adding SQUID elements to the SAA results in increased input inductance and power consumption. Adjusting the number of parallel and series SQUIDs in the SAA can optimize the SAA for a specific application.

Design properties of 90 and 150 GHz bolometers for POLARBEAR (PB) can be found in Table 1. These drive the design parameters for the DfMux readout. A notable difference between these parameters and other mm/sub-mm TES designs is the choice of a $1\ \Omega$ bolometer normal resistance. This was chosen for PB to ensure that the bolometer resistance is much greater than any of the parasitic impedances introduced by equivalent series resistance (ESR) in the capacitors and interconnects (flexible striplines, circuit board traces, connectors, etc.). Maintaining the condition $R_{\text{bolo}} \gg Z_{\text{parasitic}}$ enforces a low-impedance voltage bias on all of the bolometers across the full readout bandwidth. We then require that the photon and thermal carrier noise from the bolometer is dominant in the system which we quantify as the quadrature sum of the readout noise with the bolometer noise increasing the total system noise by 10% or less. The time constant determines the allowed bandwidth of each LC element to maintain stable operation with electrothermal feedback. Maintaining crosstalk $\leq 0.3\%$ sets the separation of each resonance frequency. The P_{sat} and operating resistance of the TES determines the amount of current that will bias each TES and must be nulled by DAN.

In this manuscript, we present a characterization of some of the properties of two NIST SAA designs, the SA4b and SA13a. Section 2 presents measurements of the transimpedance, a measure of the SAA gain when operated as a current to voltage transimpedance amplifier. Section 3 contains measurements of input inductance, which is an important parameter to consider for designing the SAA-linearizing feedback. Section 4 presents measurements of the linear range and focuses on the effective transimpedance of the amplifier in the context of large input currents, an important metric for the DfMux application. Section 5 defines an experimental measurement proto-

Table 1 Summary of POLARBEAR 90 and 150 GHz bolometer design parameters which drive the requirements on the readout system

Parameter	Value for 90 GHz bolometers	Value for 150 GHz bolometers
P_{sat}	8–9 pW	19–24 pW
R_n	1 Ω	1 Ω
T_c	420 mK	420 mK
τ_{optical}	0.4–2 ms	0.4–2 ms
\mathcal{L}	≥ 10	≥ 10
η_{optical}	$\geq 50\%$	$\geq 45\%$
Band center	89 GHz	148 GHz
Bandwidth	31%	26%

col for determining the SQUID's dynamic resistance (output resistance) and presents results. Section 6 concludes our results and presents proposed future measurements.

2 Transimpedance

As mentioned in Sect. 1, an SAA must have enough transimpedance such that the noise of the system is dominated by the photon shot noise coming from the sky signal incident on our TES bolometers.

In DfMux operation, input current is coupled to each SQUID coil in the SAA with mutual inductance M_{in} , which thereby defines the periodicity of the SAA output as a function of input current. The properties of the SAA depend on the temperature (4 K for these measurements), current and flux bias point, choices for which are shown in Fig. 3. In the DfMux system, we nominally operate the SQUID at a current bias point 0.9 times the current that gives maximum modulation depth (this increases the linear range of the SAA at the expense of some gain), and at a flux bias that maximizes the linear range of the SAA.

The gain of the SAA to small excursions from this bias point (Z) is defined by Eq. 1.

$$Z = \frac{\delta V_{\text{out}}}{\delta I_{\text{in}}} \quad (1)$$

Measured values are reported for both the SA4b and SA13a SAAs in Table 2. There was significant spread in the Z across a set of seven SA4b SAAs and two SA13a SAAs, with values ranging from 440–560 Ω for SA4b and 500–940 Ω for SA13a, all measured at 4 K. Both of these sample sets of SAAs were pre-screened to eliminate outliers with functionality problems. Larger Z values can be achieved with these SAAs by increasing the current bias and sacrificing linear range. In this case, measurements have shown $Z > 1000 \Omega$ and $Z > 600 \Omega$ for the SA13a and SA4b, respectively. However, linear range, discussed next, may be sacrificed in achieving maximum Z .

Table 2 Quantities reported here are mean values. Measurement ranges for this small sample of SAAs are reported in the above sections

SAA	Transimpedance (Ω)	Input inductance (nH)	Linear range (μA)	Dynamic resistance (Ω)
SA4	504	340	6.0	90
SA13	740	70	3.4	300

3 Linear Range

The SAA linear range is a measure of the amplitude of input signal over which the SAA is an effective amplifier. In the DfMux application, a useful definition of the linear range is the amplitude of an input signal δI_{in} over which Z remains relatively constant. This is measured by applying a low-frequency (50 kHz) AC input current of increasing amplitude and monitoring the measured Z as a function of the input amplitude. Since the gain of the SAA, Z , is a measure of the derivative of the $V-\Phi$ curve, this measurement tells you at what input flux amplitude the linear approximation in the Taylor expansion of the $V-\Phi$ about your initial flux and current bias working point is no longer sufficient to describe the response of the SQUID and nonlinear terms in the response must be added to account for the difference.¹ As δI_{in} is increased, the effective slope of the $V-\Phi$ curve decreases, decreasing the measured Z . This is illustrated in Fig. 4a.

A measurement of this effect for this set of SA4 SAAs is shown in Fig. 4b. The oscillating behavior in the tail of the function in Fig. 4b can be understood in the cartoon in Fig. 4a as the signal exploring multiple periods of the $V-\Phi$ curve. Noted on the plot as the linear range is the input current amplitude δI_{in} at which the transimpedance drops to 90% of its maximum value. At this point, in a Taylor expansion about the maximum transimpedance point in the $V-\Phi$ s the linear term in the expansion is ~ -1.0 , the quadratic term is $\sim 1 \times 10^{-5}$, and the cubic term is ~ 0.1 . Measured in this way, the linear range is found to be 5.6–6.9 μA for SA4b and 3.4–3.5 μA for SA13a. Average results are given in Table 2. Note that this linear range is *without* any enhancement due to feedback. Additionally, there is an optimization in linear range with respect to bias current. The bias current that gives you the maximum Z does not give you the maximum linear range. This is illustrated in Fig. 5, which estimates linear range at Z as a function of current bias using a Taylor expansion of each of the $V-\Phi$ curves shown in Fig. 6 about the input coil flux that maximizes Z (following the methodology in The SQUID Handbook). Defining linear range as the deviation in input coil current from the working point at which the higher-order Taylor expansion terms drop Z by 0.9 (following the definition above) leads to Fig. 5.

¹ The SQUID Handbook [9] defines linear range in terms of a Taylor expansion of the $V-\Phi$ curve—we do not derive our linear range from $V-\Phi$ curves, but our measurement is a way of probing the relative contributions of higher-order terms in this expansion.

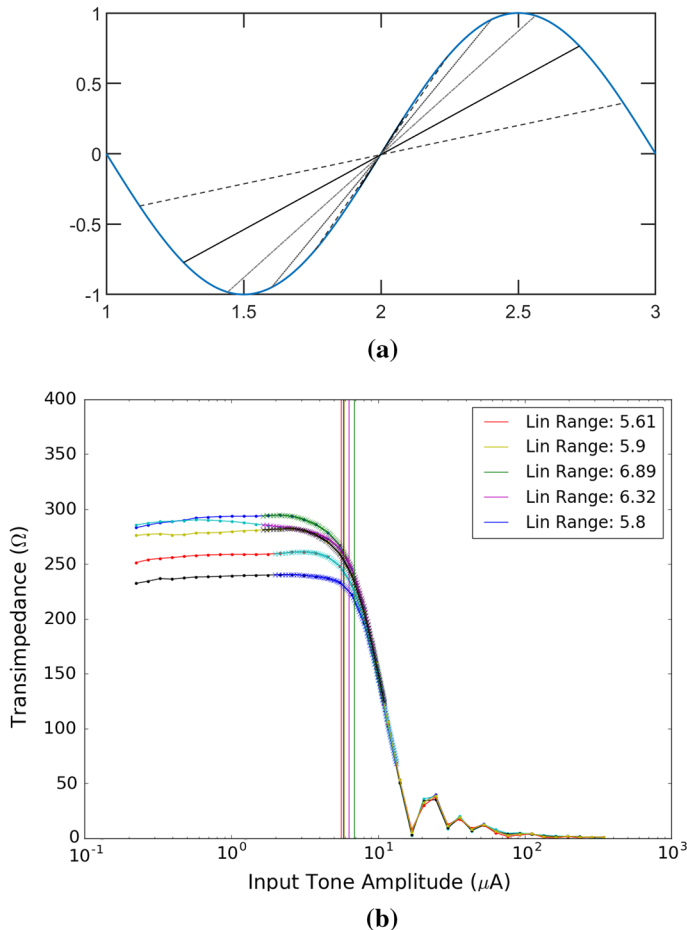


Fig. 4 **a** Illustration of transimpedance ($V-\Phi$ slope) decreasing as flux burden amplitude increases. Different line styles are demonstrating various amplitude input signals about the working point. The output signal increases roughly linearly with the input signal in a narrow flux range about the operating point, but as the flux range increases too far from the working point, the gain (slope of the black + gray lines) drops dramatically. **b** Linear range defined as point where transimpedance drops to 90% of its maximum value (Color figure online)

4 Input Inductance

Inductance of the input coil of the SAA is an important property to measure because it presents a parasitic impedance in series with the TES bolometers with magnitude increasing with frequency. The DfMux Digital Active Nulling (DAN) [8] both increases the linear range of the SAA and decreases the input impedance of the SAA presented to the bolometer circuit. However, the input impedance of the SAA remains an important circuit parameter, with lower values providing increased performance, because of the finite impedance of the sub-Kelvin detector circuit Z_{comb} . DAN performs feedback via a comb of amplitude-modulated nulling tones with a channel

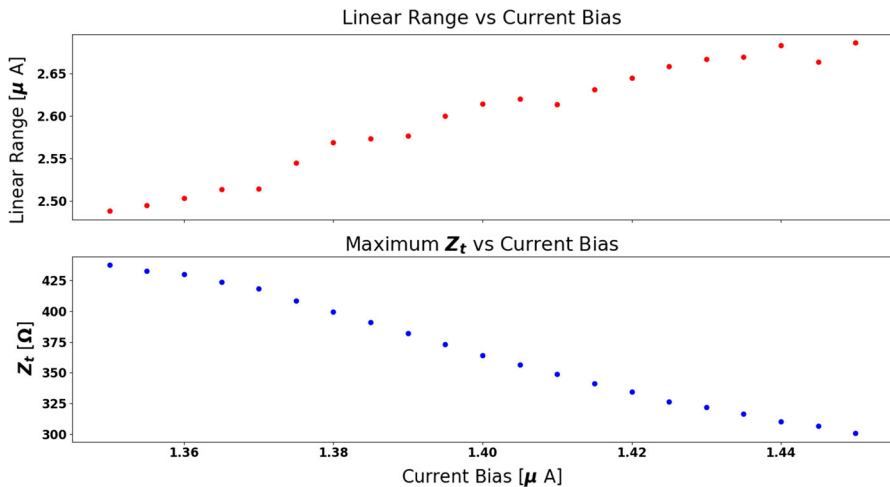
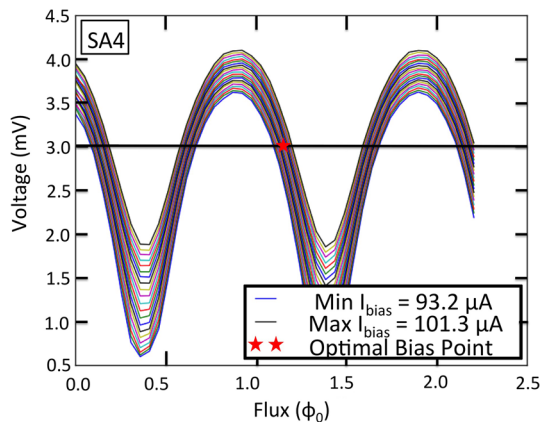


Fig. 5 Taylor expanding the family of $V-\Phi$ curves at difference current biases (shown in Fig. 6) shows that there is a trade off in gain and linearity (Color figure online)

Fig. 6 $V-\Phi-I$ manifold with the operational bias point shown as a red star. Each curve is a $V-\Phi$ curve at fixed I_{bias} . The black line shows the fixed voltage for which $\frac{d\Phi}{dT}$ is calculated (Color figure online)



bandwidth of ~ 1 kHz. These tones are fed back as a current to the input coil of the SQUID (as opposed to flux feedback which uses a separate feedback transformer). Within the bandwidth of a DAN channel, this nulling current sums with the carrier bias current to create the virtual ground at the input to the SAA. The amplitude modulation of nulling current required to create this virtual ground is the DfMux measurement of the bolometer signal, including any noise sources originating with the carrier or in the bolometer. Noise sources within the SAA or anywhere in the feedback path (see Fig. 1) similarly cause a nuller signal, but that signal is not meeting an equal and opposite signal at the input of the SAA, and so does not see a virtual ground at the input to the SAA. These nuller signals without anything to null split between the input coil and the bolometer circuit. Only the current that goes through the SAA actually acts to reduce the error signal coming out of the SAA, so reducing this error signal requires a current I_{null} related to any noise current in the bolometer feedback path I_{in}

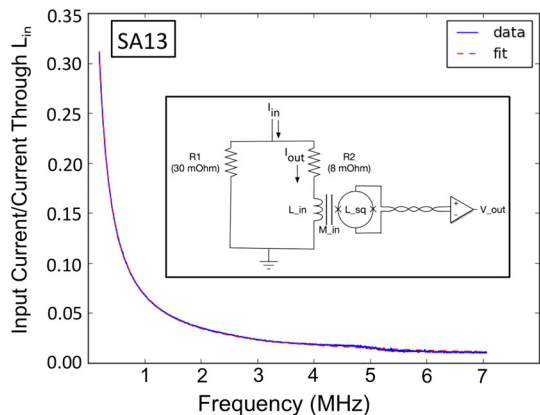
by Eq. 2. In this equation, Z_{in} is the input impedance of the SAA including parasitic inductances associated with the wirebonds from the SAA mounting PCB to the input coil of the SAA and the inductance of the circuit board traces between the input coil bond pads and the nulling point on the mounting PCB (in total $L_{parasitic} \sim 20$ nH). Z_{comb} is the impedance of the LC comb which includes the parallel combination of all LC branches (where each branch consists of a series combination of R_{bolo} , $L_{resonator}$, $C_{resonator}$, and the equivalent series resistance of the capacitors) as well as parasitic capacitance in parallel with the comb (~ 2 nF), and parasitic inductance in series with the comb from the flexible striplines connecting the 4 K SAA PCB to the LC combs (~ 40 nH [10]).

$$I_{in} = I_{null} \left(1 + \frac{Z_{in}}{Z_{comb}} \right) \quad (2)$$

This means that noise with its origin in the feedback path, as measured by the amount of nuller required to bring the error signal to zero, depends on SAA input impedance as shown in Eq. 2. This type of noise is reduced in three ways: (1) reduction in the enhancement factor $(1 + \frac{Z_{in}}{Z_{comb}})$ by either reducing Z_{in} or increasing Z_{comb} , (2) reduction in the amount of noise that is introduced between the summing point and the input to the ADC (300 K Amplifier Noise, SAA Flux Noise, ADC quantization noise and Johnson noise from wiring and gain setting resistors), and (3) by moving the feedback closer to the SQUID. The other options are being actively explored; here we address option (1) by presenting data on the SAA input inductance for the two SAA's under investigation.

The SAA input inductance is measured using the circuit shown in the inset in Fig. 7. This circuit produces a single pole rolloff in the measured output of the SAA as input current is shunted away from the SAA through $R1$ more effectively at higher frequencies. The fit of data from a single SA13a SAA is shown in Fig. 7. The input inductance measured in this way is 340 nH for SA4b and 70 nH for SA13a, also given in Table 2. These reported values include stray inductance associated with wirebonds and PCB traces which we expect to be ~ 20 nH independent of the SAA.

Fig. 7 Inset: circuit diagram of input inductance measurement. Graph: data and fit to single pole transfer function for SA13 (Color figure online)



5 Dynamic Resistance

The dynamic resistance (R_{dyn}) is the measure of the output resistance of the SAA, a quantity of interest when optimally matching it to follow-on components such as wiring and amplifiers. The definition of dynamic resistance used here is

$$R_{\text{dyn}} = \frac{dV}{d\Phi} \bigg|_I \frac{d\Phi}{dI} \bigg|_V. \quad (3)$$

R_{dyn} is measured by analyzing $V-\Phi$ in a finely sampled range of current biases around the operational current bias point to produce a $V-\Phi-I$ space. The derivatives in Eq. 3 are then evaluated using finite differences in this data. R_{dyn} was measured on one SA4b and SA13a, each at 4 K. Like Z , this number depends on the operating temperature and bias point in the $V-\Phi-I$ space. R_{dyn} is measured to be $90\ \Omega$ for SA4b, and $300\ \Omega$ for SA13a. Measurements reported here (in Table 2) are for the same conditions as the Z measurements, described above.

6 Conclusion

We outlined measurement techniques and results for transimpedance, linear range, dynamic range, and dynamic resistance of two NIST design SAAs, the SA4b and SA13a. These results are summarized in Table 2. Future work includes measurements of white noise (previously reported for both models in [2,11]), magnetic field sensitivity, and dependence of the quantities reported here on operating point and temperature. Minimizing noise associated with the feedback circuit described in Sect. 4 is also actively being studied including design and testing of optimized two stage SQUID architectures like that used in XIFU and Safari [12].

Acknowledgements SQUID arrays used in this work were fabricated in the NIST-Boulder microfabrication facility. DfMux room-temperature digital electronics used for these measurements were built by the McGill Cosmology Group. DB is supported by an NSF Astronomy and Astrophysics Postdoctoral Fellowship under Award AST-1501422.

References

1. M. Dobbs, N. Halverson, P. Ade, K. Basu, A. Beelen, F. Bertoldi, C. Cohalan, H. Cho, R. Güsten, W. Holzapfel, Z. Kermish, R. Kneissl, A. Kovács, E. Kreysa, T. Lanting, A. Lee, M. Lueker, J. Mehl, K. Menten, D. Muders, M. Nord, T. Plagge, P. Richards, P. Schilke, D. Schwan, H. Spieler, A. Weiss, M. White, Apex-sz first light and instrument status. *New Astron. Rev.* **50**(11), 960–968 (2006)
2. R.P. Welty, J.M. Martinis, Two-stage integrated squid amplifier with series array output. *IEEE Trans. Appl. Supercond.* **3**, 2605–2608 (1993)
3. J. Hubmayr, F. Aubin, E. Bissonnette, M. Dobbs, S. Hanany, A.T. Lee, K. MacDermid, X. Meng, I. Sagiv, G. Smecher, Design and characterization of tes bolometers and squid readout electronics for a balloon-borne application. *Proc. SPIE* **7020**, 7020–7020-8 (2008)
4. B.A. Benson, P.A.R. Ade, Z. Ahmed, S.W. Allen, K. Arnold, J.E. Austermann, A.N. Bender, L.E. Bleem, J.E. Carlstrom, C.L. Chang, H.M. Cho, J.F. Cliche, T.M. Crawford, A. Cukierman, T. de Haan, M.A. Dobbs, D. Dutcher, W. Everett, A. Gilbert, N.W. Halverson, D. Hanson, N.L. Harrington, K. Hattori, J.W. Henning, G.C. Hilton, G.P. Holder, W.L. Holzapfel, K.D. Irwin, R. Keisler, L. Knox,

- D. Kubik, C.L. Kuo, A.T. Lee, E.M. Leitch, D. Li, M. McDonald, S.S. Meyer, J. Montgomery, M. Myers, T. Natoli, H. Nguyen, V. Novosad, S. Padin, Z. Pan, J. Pearson, C. Reichardt, J.E. Ruhl, B.R. Saliwanchik, G. Simard, G. Smecher, J.T. Sayre, E. Shirokoff, A.A. Stark, K. Story, A. Suzuki, K.L. Thompson, C. Tucker, K. Vanderlinde, J.D. Vieira, A. Vikhlinin, G. Wang, V. Yefremenko, K.W. Yoon, Spt-3g: a next-generation cosmic microwave background polarization experiment on the south pole telescope. *Proc. SPIE* **9153**, 9153–9153-21 (2014)
5. J.E. Austermann, K.A. Aird, J.A. Beall, D. Becker, A. Bender, B.A. Benson, L.E. Bleem, J. Britton, J.E. Carlstrom, C.L. Chang, H.C. Chiang, H.-M. Cho, T.M. Crawford, A.T. Crites, A. Datsman, T. de Haan, M.A. Dobbs, E.M. George, N.W. Halverson, N. Harrington, J.W. Henning, G.C. Hilton, G.P. Holder, W.L. Holzapfel, S. Hoover, N. Huang, J. Hubmayr, K.D. Irwin, R. Keisler, J. Kennedy, L. Knox, A.T. Lee, E. Leitch, D. Li, M. Lueker, D.P. Marrone, J.J. McMahon, J. Mehl, S.S. Meyer, T.E. Montroy, T. Natoli, J.P. Nibarger, M.D. Niemack, V. Novosad, S. Padin, C. Pryke, C.L. Reichardt, J.E. Ruhl, B.R. Saliwanchik, J.T. Sayre, K.K. Schaffer, E. Shirokoff, A.A. Stark, K. Story, K. Vanderlinde, J.D. Vieira, G. Wang, R. Williamson, V. Yefremenko, K.W. Yoon, O. Zahn, Sptpol: an instrument for cmb polarization measurements with the south pole telescope. *Proc. SPIE* **8452**, 8452–8452-18 (2012)
 6. Z.D. Kermish, P. Ade, A. Anthony, K. Arnold, D. Barron, D. Boettger, J. Borrill, S. Chapman, Y. Chinone, M.A. Dobbs, J. Errard, G. Fabbian, D. Flanigan, G. Fuller, A. Ghrabi, W. Grainger, N. Halverson, M. Hasegawa, K. Hattori, M. Hazumi, W.L. Holzapfel, J. Howard, P. Hyland, A. Jaffe, B. Keating, T. Kisner, A.T. Lee, M.L. Jeune, E. Linder, M. Lungu, F. Matsuda, T. Matsumura, X. Meng, N.J. Miller, H. Morii, S. Moyerman, M.J. Myers, H. Nishino, H. Paar, E. Quealy, C.L. Reichardt, P.L. Richards, C. Ross, A. Shimizu, M. Shimon, C. Shimmmin, M. Sholl, P. Siritanasak, H. Spieler, N. Stebor, B. Steinbach, R. Stompor, A. Suzuki, T. Tomaru, C. Tucker, O. Zahn, The polarbear experiment. *Proc. SPIE* **8452**, 8452–8452-15 (2012)
 7. A. Suzuki, P. Ade, Y. Akiba, C. Aleman, K. Arnold, C. Baccigalupi, B. Barch, D. Barron, A. Bender, D. Boettger, J. Borrill, S. Chapman, Y. Chinone, A. Cukierman, M. Dobbs, A. Ducout, R. Dunner, T. Elleflot, J. Errard, G. Fabbian, S. Feeney, C. Feng, T. Fujino, G. Fuller, A. Gilbert, N. Goeckner-Wald, J. Groh, T.D. Haan, G. Hall, N. Halverson, T. Hamada, M. Hasegawa, K. Hattori, M. Hazumi, C. Hill, W. Holzapfel, Y. Hori, L. Howe, Y. Inoue, F. Irie, G. Jaehnig, A. Jaffe, O. Jeong, N. Katayama, J. Kaufman, K. Kazemzadeh, B. Keating, Z. Kermish, R. Keskitalo, T. Kisner, A. Kusaka, M.L. Jeune, A. Lee, D. Leon, E. Linder, L. Lowry, F. Matsuda, N. Matsumura, N. Miller, K. Mizukami, J. Montgomery, M. Navaroli, H. Nishino, J. Peloton, D. Poletti, G. Puglisi, G. Rebeiz, C. Raun, C. Reichardt, P. Richards, C. Ross, K. Rotermund, Y. Segawa, B. Sherwin, I. Shirley, P. Siritanasak, N. Stebor, R. Stompor, J. Suzuki, O. Tajima, S. Takada, S. Takakura, S. Takatori, A. Tikhomirov, T. Tomaru, B. Westbrook, N. Whitehorn, T. Yamashita, A. Zahn, O. Zahn, The polarbear-2 and the simons array experiments. *J. Low Temp. Phys.* **184**, 805–810 (2016)
 8. M.A. Dobbs, M. Lueker, K.A. Aird, A.N. Bender, B.A. Benson, L.E. Bleem, J.E. Carlstrom, C.L. Chang, H.-M. Cho, J. Clarke, T.M. Crawford, A.T. Crites, D.I. Flanigan, T. de Haan, E.M. George, N.W. Halverson, W.L. Holzapfel, J.D. Hrubes, B.R. Johnson, J. Joseph, R. Keisler, J. Kennedy, Z. Kermish, T.M. Lanting, A.T. Lee, E.M. Leitch, D. Luong-Van, J.J. McMahon, J. Mehl, S.S. Meyer, T.E. Montroy, S. Padin, T. Plagge, C. Pryke, P.L. Richards, J.E. Ruhl, K.K. Schaffer, D. Schwan, E. Shirokoff, H.G. Spieler, Z. Staniszewski, A.A. Stark, K. Vanderlinde, J.D. Vieira, C. Vu, B. Westbrook, R. Williamson, Frequency multiplexed superconducting quantum interference device readout of large bolometer arrays for cosmic microwave background measurements. *Rev. Sci. Instrum.* **83**(7), 073113 (2012)
 9. J. Clarke, A.I. Braginski, *The SQUID Handbook Fundamentals and Technology of SQUIDS and SQUID Systems* (Wiley, Weinheim, 2006)
 10. J.S. Avva, P.A.R. Ade, Z. Ahmed, A.J. Anderson, J.E. Austermann, R.B. Thakur, D. Barron, A.N. Bender, B.A. Benson, J.E. Carlstrom, F.W. Carter, T. Cecil, C.L. Chang, J.F. Cliche, A. Cukierman, E.V. Denison, T. de Haan, J. Ding, M.A. Dobbs, D. Dutcher, T. Elleflot, W. Everett, A. Foster, R.N. Gannon, A. Gilbert, J.C. Groh, N.W. Halverson, A.H. Harke-Hosemann, N.L. Harrington, M. Hasegawa, K. Hattori, J.W. Henning, G.C. Hilton, W.L. Holzapfel, Y. Hori, N. Huang, K.D. Irwin, O.B. Jeong, M. Jonas, T. Khaire, A.M. Kofman, M. Korman, D. Kubik, S. Kuhlmann, C.L. Kuo, A.T. Lee, A.E. Lowitz, S.S. Meyer, J. Montgomery, A. Nadolski, T. Natoli, H. Nguyen, G.I. Noble, V. Novosad, S. Padin, Z. Pan, J. Pearson, C.M. Posada, A. Rahlin, K. Rotermund, J.E. Ruhl, L.J. Saunders, J.T. Sayre, I. Shirley, E. Shirokoff, G. Smecher, J.A. Sobrin, A.A. Stark, K.T. Story, A. Suzuki, Q.Y. Tang, K.L. Thompson, C. Tucker, L.R. Vale, K. Vanderlinde, J.D. Vieira, G. Wang, N. Whitehorn, V. Yefremenko,

- K.W. Yoon, M.R. Young, Design and assembly of SPT-3G cold readout hardware. *J. Low Temp. Phys.* (2018). <https://doi.org/10.1007/s10909-018-1965-5>
11. W.B. Doriese, K.M. Morgan, D.A. Bennett, E.V. Denison, C.P. Fitzgerald, J.W. Fowler, J.D. Gard, J.P. Hays-Wehle, G.C. Hilton, K.D. Irwin, Y.I. Joe, J.A.B. Mates, G.C. O'Neil, C.D. Reintsema, N.O. Robbins, D.R. Schmidt, D.S. Swetz, H. Tatsuno, L.R. Vale, J.N. Ullom, Developments in time-division multiplexing of X-ray transition-edge sensors. *J. Low Temp. Phys.* **184**, 389–395 (2016)
 12. L. Gottardi, M. Kiviranta, J. van der Kuur, H. Akamatsu, M.P. Bruijn, R. den Hartog, Nearly quantum limited two-stage squid amplifiers for the frequency domain multiplexing of tes based X-ray and infrared detectors. *IEEE Trans. Appl. Supercond.* **25**, 1–4 (2015)